Chem

Article

Synthesis of single-crystalline carbon nanothreads from 1-naphthoic acid with high anisotropic thermal conductivity

Graphical abstract

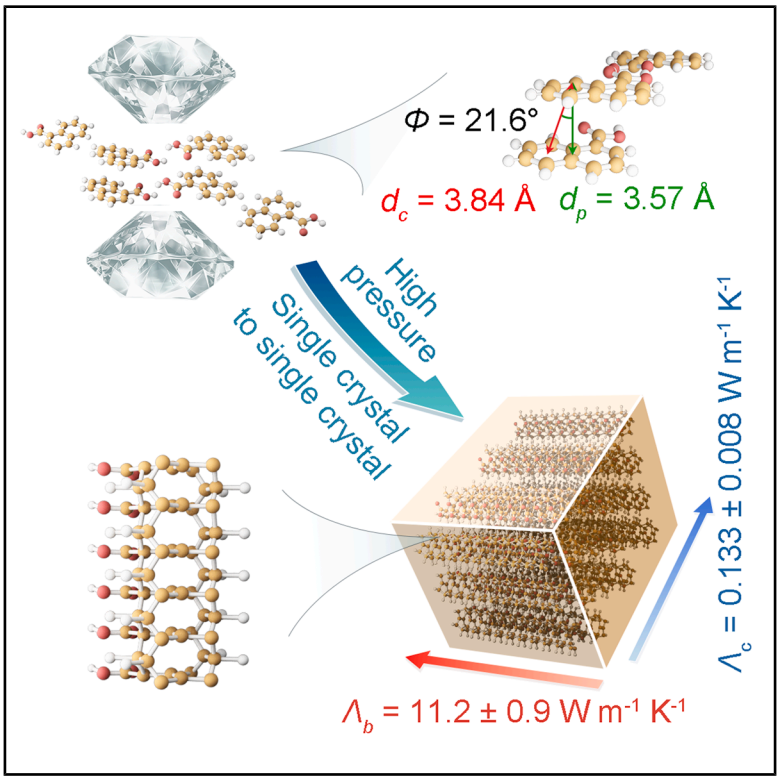

Highlights

- Bulk synthesis of a carbon nanothread single crystal
- Single-crystal-to-single-crystal transformation
- Exceptional compressive resistance along the thread axis
- Strongly anisotropic thermal conductivity along and perpendicular to the thread

Authors

Xin Yang, Qingchao Zeng, Yizhe Liu, ..., George D. Cody, Ho-kwang Mao, Kuo Li

Correspondence

likuo@hpstar.ac.cn

In brief

Employing a design strategy focused on single-crystal-to-single-crystal transformation, we synthesized high-quality carbon nanothread single crystals from 1-naphthoic acid by using high-pressure and annealing approaches. The resultant single crystal demonstrates remarkable compressive resistance along the thread axis, as well as highly anisotropic thermal conductivity parallel and perpendicular to the thread direction with a value of around 84. These results provide novel insights for the design and synthesis of low-dimensional carbon materials featuring unique topologies and properties.

Yang et al., 2026, Chem *12*, 102836
May 14, 2026
https://doi.org/10.1016/j.chempr.2025.102836

CellPress

Please cite this article in press as: Yang et al., Synthesis of single-crystalline carbon nanothreads from 1-naphthoic acid with high anisotropic thermal conductivity, Chem (2025), https://doi.org/10.1016/j.chempr.2025.102836

Chem

CellPress

Article

Synthesis of single-crystalline carbon nanothreads from 1-naphthoic acid with high anisotropic thermal conductivity

Xin Yang,[1,8] Qingchao Zeng,[1,8] Yizhe Liu,[2] Bo Sun,[2,3] Ruyue Shi,[1] Xingyu Tang,[1] Guangwei Che,[1] Peijie Zhang,[1] Haiyan Zheng,[1] Yajie Wang,[1] Aijiao Guan,[4] Junfeng Xiang,[4] Dexiang Gao,[1] Xuan Wang,[1] Yida Wang,[1] Yongjin Chen,[1] Xiao Dong,[5] George D. Cody,[6] Ho-kwang Mao,[1,7] and Kuo Li[1,9,*]

[1]Center for High Pressure Science and Technology Advanced Research, Beijing 100193, P.R. China
[2]Tsinghua Shenzhen International Graduate School, Tsinghua University, Shenzhen 518055, P.R. China
[3]Guangdong Provincial Key Laboratory of Thermal Management Engineering & Materials, Shenzhen 518055, P.R. China
[4]Institute of Chemistry, Chinese Academy of Science, Beijing 100190, P.R. China
[5]Key Laboratory of Weak-Light Nonlinear Photonics, School of Physics, Nankai University, Tianjin 300071, P.R. China
[6]Geophysical Lab, Carnegie Institution of Washington, 5251 Broad Branch Road NW, Washington, DC 20015, USA
[7]Shanghai Key Laboratory of MFree, Shanghai Advanced Research in Physical Sciences, Shanghai 201203, P.R. China
[8]These authors contributed equally
[9]Lead contact
*Correspondence: likuo@hpstar.ac.cn
https://doi.org/10.1016/j.chempr.2025.102836

THE BIGGER PICTURE Diamond-family materials have unparalleled mechanical, electronic, and thermal conductive properties, making them promising candidate materials for next-generation semiconductors. At only a couple of carbon atoms thick, sp^3-carbon nanothreads (CNThs), also called diamond nanothreads, are predicted to have even greater stiffness than carbon nanotubes and excellent anisotropic thermal conductivity. These properties allow them to direct heat transport in the desired direction rather than an unwanted one. However, the synthesis of high-quality CNTh materials is still a huge challenge, prohibiting experimental investigation of their properties and practical applications. Here, we have successfully synthesized a 100-μm-scale CNTh single crystal via single-crystal-to-single-crystal transformation of 1-naphthoic acid under high pressure. The CNTh has a pseudo-hexagonal diamond structure, and its large size allowed us to experimentally reveal the highly anisotropic thermal conductivity ($\Lambda_{\parallel}/\Lambda_{\perp} \approx 84$) and close-to-zero compressibility along the thread. Our results also demonstrated the scalable preparation of CNThs with excellent crystallinity, paving the way for designing and synthesizing atom-scale ordered diamond-family nanomaterials.

SUMMARY

Carbon nanothreads (CNThs) are one-dimensional diamondoid nanomaterials. They are predicted to combine diamonds' high strength and thermal conductivity with enhanced flexibility, but current synthesis methods struggle to produce high-quality single-crystalline CNThs. Here, we report the synthesis of a 100-μm-scale CNTh single crystal via a single-crystal-to-single-crystal transformation by compressing 1-naphthoic acid at 20 GPa and 573 K. Structurally, the CNTh resembles a hexagonal diamond. The intrathread bonding is governed by a sequential regioselective Diels-Alder reaction, and hydrogen bonds control the interthread ordering. The large, high-quality crystal allowed the experimental demonstration of the highly anisotropic compressibility and thermal conductivity. The thermal conductivity was 11.2 W m^{-1} K^{-1} along the thread, 84 times greater than across it, and a near-zero compressibility along the thread, in contrast to 0.013 GPa^{-1} across the thread. CNThs are therefore demonstrated as anisotropic thermal conductive materials with excellent mechanical properties.

INTRODUCTION

Diamonds are recognized as fourth-generation semiconductors because of their ultra-wide band gap, exceptional mechanical hardness,[1] remarkable thermal conductivity,[2] superior charge-carrier mobility,[3,4] and high dielectric breakdown strength.[4] Alongside their chemical inertness and biocompatibility,[5] these properties position diamonds as promising materials in electronics

Please cite this article in press as: Yang et al., Synthesis of single-crystalline carbon nanothreads from 1-naphthoic acid with high anisotropic thermal conductivity, Chem (2025), https://doi.org/10.1016/j.chempr.2025.102836

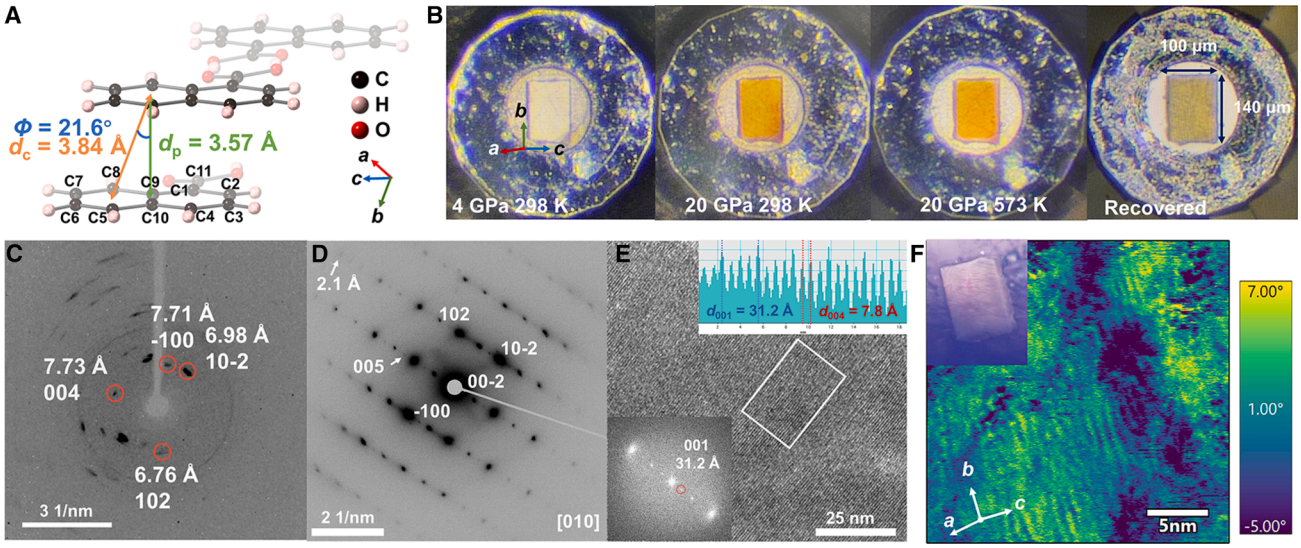

Figure 1. Structure of 1-NA and 1-NA CNTh

(A) Geometric parameters of local π-stacking of 1-NA with an interplane distance of d_p = 3.57 Å, a ring-center distance of d_c = 3.84 Å (along *b* axis), and a slip angle of Φ = 21.6°.

(B) Optical images of a 1-NA single crystal during compression. The stacking direction, *b* axis, is along the crystal's longest edge.

(C) Selected 2D SCXRD pattern of 1-NA CNTh. Because the X-ray beam can cover the whole crystal, the lattice is uniform across the whole crystal.

(D) SAED pattern of 1-NA CNTh with the minimum *d*-spacing of 2.1 Å.

(E) HRTEM image of 1-NA CNTh. The adjacent thread spacing of 7.8 Å is attributed to the (004) plane. The insets show the profile across the threads and the fast Fourier transform (FFT) image.

(F) AFM image of a 1-NA CNTh single crystal with phase imaging mode. The inset shows the optical image of the scanned crystal surface in the same orientation. The surface shown was identified as (104) by SCXRD (see Figure S5A).

and other advanced applications. In addition to the well-known conventional bulk diamonds, recent advances have led to the discovery of lower-dimensional diamond allotropes, such as two-dimensional diamane,[6] which represent nanometer-thick diamond films with hydrogen terminals. Carbon nanothreads (CNThs), sp^3-bonded one-dimensional diamondoid nanomaterials that have only a few carbon atoms across their cross-section and a hydrogen-terminated surface, are proposed to combine the advantages of diamonds with the flexibility of polymers.[7–10] They are predicted to have a Young's moduli greater than 1.5 TPa,[7] a band gap of 3.5–4.8 eV,[10] a thermal conductivity reaching up to 10^3 W m^{-1} K^{-1},[11] a tenacity of 4.1 × 10^7 N m kg^{-1},[12] and a mass sensitivity of 0.58 × 10^{-24} g as a resonator.[13] As insulated counterparts to carbon nanotubes, CNThs have potential in nanomechanical systems and applications for nanoscale heat management requiring highly anisotropic thermal conductivity. Although many scientific and engineering applications have been proposed,[13–16] they remain unexplored because of the huge challenge in preparing large, high-quality CNTh crystals.

Fitzgibbons et al. synthesized the first CNThs in 2015 by compressing benzene to 20 GPa at room temperature.[9] The product exhibited significant bonding disorders, alongside amorphous side products, which arose as a result of the competing polymerization pathways of benzene, such as Diels-Alder and [1,4]-polymerization reactions.[17–20] Great efforts have thus been devoted to improving the ordering of CNTh, including modifying precursor molecules with heteroatoms (e.g., furan,[21] thiophene,[22] s-triazine,[23] pyridine,[24] and pyridazine[25]) to enhance selectivity and introducing a fused-ring structure or hydrogen bond to stabilize the stacking (e.g., $C_{10}F_8$-$C_{10}F_8$ and $C_{14}H_{10}$-$C_{10}F_8$ co-crystals,[26,27] phenol:pentafluorophenol co-crystals,[28] phenol,[29] aniline,[30] and 2,5-furandicarboxylic acid[31,32]). A recent review summarized the efforts over the past decade.[33] Although some report single-crystal diffraction spots in high-pressure synchrotron X-ray diffraction (XRD) experiments,[26,27] obtaining a CNTh single-crystal sample for subsequent research at ambient pressure remains challenging, limiting the investigation of its unique physical properties.

1-Naphthoic acid (1-NA), a monocarboxylic derivative of naphthalene, combines carboxylic and bicyclic skeletons, which is a potential candidate for synthesizing double-ring CNThs with higher defect tolerance and higher 1D ultimate strength and bending modulus.[34,35] Under ambient conditions, 1-NA crystallizes in a monoclinic lattice with parameters *a* = 6.91 Å, *b* = 3.84 Å, *c* = 30.97 Å, and β = 92.01°. The molecules form dimers through strong hydrogen bonds, and these dimers are slip-stacked in columns along the *b* axis. The key parameter for measuring molecular stacking is the slip angle Φ,[36] which is 21.6° (Figure 1A), significantly smaller than the 61.32° for benzene[36] and 65.8° for aniline[37] and close to 28.1° for 2,5-furandicarboxylic acid.[31] This indicates more effective π-stacking in 1-NA, which helps to preserve crystallinity during polymerization together with the intermolecular hydrogen bonds.

The single-crystal-to-single-crystal topochemical polymerization provides a promising solution for creating a large single-crystal polymer by light or heating initiation.[38–40] Complementary

to heating or high-energy photon irradiation, high-pressure solid-state polymerization provides a constrained environment for constructing materials with a dense extended structure, dramatically enhancing the intermolecular interactions.[41–43] Here, we successfully synthesized a 100-μm-scale CNTh single crystal via a single-crystal-to-single-crystal transformation of 1-NA at 20 GPa and 573 K, which can be viewed as a huge bundle of nanothreads that were orderly stacked. The high inter/intra-thread order stems from robust carboxyl-carboxyl hydrogen bonding and distinct reactivity between γ-C and β-C. The large size of the 1-NA CNTh crystal allowed us to measure the thermal conductivity and compressibility. The thermal conductivities along and across the thread were both very close to the predicted values and showed strong anisotropy. The ratio between conductivity along the fast axis (Λ_f, along the thread) and that along the slow axis (Λ_s, across the thread) reached ~84, close to that of the hexagonal boron nitride.[44] Our work demonstrates the synthesis of large CNTh single crystals, a material class that plays a foundational role in the design of anisotropic 1D devices, such as heat spreaders in microelectronics.

RESULTS

Synthesis and interthread structure of the 1-NA CNTh single crystal

The synthesis of CNTh single-crystal benefits from the effective pre-stacking of 1-NA molecules and slow hydrostatic compression combined with annealing. *In situ* high-pressure, room-temperature spectroscopic and XRD experiments revealed that 1-NA begins to polymerize at 15 GPa and completes around 20 GPa (Figures S1–S3). Then, we loaded a piece of 1-NA single crystal into a diamond anvil cell (DAC) with Ne as a pressure-transmitting medium. The crystal had a rectangular shape, and the *b* axis was along the long edge, as shown in Figure 1B. After testing various conditions, we found that 20 GPa and 573 K provided the optimal parameters for producing a high-quality single-crystal product. Higher pressure increased the risk of crystal fragmentation, and 573 K represented a moderate temperature that was not only readily attainable but also effective in relieving internal stresses generated during the reaction, thereby minimizing crystal defects. The sample was first compressed to 20 GPa at 1 GPa/h and subsequently annealed at 573 K for 3 h before being released to ambient conditions. The *in situ* infrared (IR) spectra of single-crystal 1-NA showed that, after the sample was heated to 573 K at 20 GPa, the intensity of sp^3 C–H stretching increased, indicating that heat can also accelerate the reaction (Figure S4). A yellowish single-crystal product of 140 × 100 × 20 μm^3 was finally obtained (Figure 1B). The obtained crystal was subsequently characterized outside the DAC by a lab single-crystal X-ray diffractometer (SCXRD). The bright diffraction spots (Figure 1C) were indexed as *h*0*l* of a 2D lattice with a = 7.71 Å, c = 30.92 Å, and β = 92°. The absence of *b* axis information (Figure S5B) most likely resulted from random interthread shifts. These results are also consistent with the characteristic lattices from selected-area electron diffraction (SAED; Figure 1D) and powder XRD data from a polycrystalline product synthesized by a Paris-Edinburgh (PE) press under 20 GPa (PE20; Figure S5C). This lattice approximately inherited that of 1-NA and clearly indicates a topochemical single-crystal-to-single-crystal polymerization along the *b* axis. In real space, the stacked threads were directly observed by high-resolution transmission electron microscopy (HRTEM; Figure 1E) and atomic force microscopy (AFM; Figure 1F). Among the optical images of the single-crystal product (the inset of Figure 1F), the AFM image clearly shows that the threads extended along the long axis (*b* axis). The well-defined lattice parameters obtained from SCXRD indicate that 1-NA CNTh has excellent ordering in stacking across the whole crystal. Achieving such ordering was previously challenging. The reported CNThs recovered to ambient pressure often lacked long-range order and exhibited only broad or weak first-order diffractions around d = 5.6 Å.[17,24,30]

Local structure of 1-NA CNTh and the topochemical polymerization process

The local structure of CNThs is closely related to their physical properties. Because the XRD and IR data showed that polycrystalline product PE20 is consistent with the single-crystal product (Figure S6), we carefully studied the local structure of 1-NA CNTh via solid-state nuclear magnetic resonance (ssNMR) and pair-distribution function (PDF). We performed high-resolution ^{13}C cross-polarization (CP) (^1H-^{13}C) total sideband suppression (CPTOSS) (black line in Figure S7A) and non-quaternary suppression (NQS) ssNMR spectroscopy (orange line in Figure S7A). CPTOSS revealed both the hydrogenated and non-hydrogenated carbons, whereas NQS ssNMR showed only the quaternary carbon. By comparing these two results, we identified five types of carbon atoms: the carboxyl carbon (C11, 174 ppm), non-hydrogenated carbons C=C-R2 (134 ppm) and $\underline{C}$-R_4 (50 ppm), and hydrogenated carbons C=$\underline{C}$H-R (128 ppm) and H–$\underline{C}$-R_3 (41 ppm). By enumerating the possible positions of the unreacted carbons and calculating their ^{13}C chemical shifts, we determined that double bonds are located only between certain β-C (C2=C3 and C6=C7, 128 ppm) and γ-C (C9=C10, 134 ppm) (Figure S8; the dominated local structures are highlighted by the check mark). α-C (C1,4,5,8) transferred into sp^3-C completely with C1 at 50 ppm and C(4,5,8) at 41 ppm. The saturated C(9,10) also contributed to the peak at 50 pm, and the saturated C(2,3,6,7) contributed to the peak at 41 ppm.

Then, we quantified the high-pressure reactivity of carbon atoms in 1-NA by collecting and fitting the fully relaxed direct-polarization (DP) ^{13}C NMR spectrum (Figures 2A and S7B–S7H). As calculated, 100% of α-C and 74% of β-C (27.8/(27.8 + 10.0)) transformed into sp^3-C, whereas only 28% of γ-C (4.6/(4.6 + 11.6)) reacted, indicating that α-C and β-C are much more reactive than γ-C. Given that the four α- and β-C in each ring of 1-NA form a diene—like that in furan,[21] thiophene,[22] and 1,2-diazine[25]—we deduced that the polymerization proceeds via a sequential Diels-Alder reaction and dominatingly produces an unsaturated hexagonal diamond (uHD) nanothread. Compared with the hexagonal diamond (HD) structure, the unsaturated 1-NA CNTh has its axis aligned along the [100] direction of HD. Therefore, it is referred to as uHD[100] (Figure 2B). This structure is also evident in Figure 2A, which compares the experimental NMR data with the simulation result.

Please cite this article in press as: Yang et al., Synthesis of single-crystalline carbon nanothreads from 1-naphthoic acid with high anisotropic thermal conductivity, Chem (2025), https://doi.org/10.1016/j.chempr.2025.102836

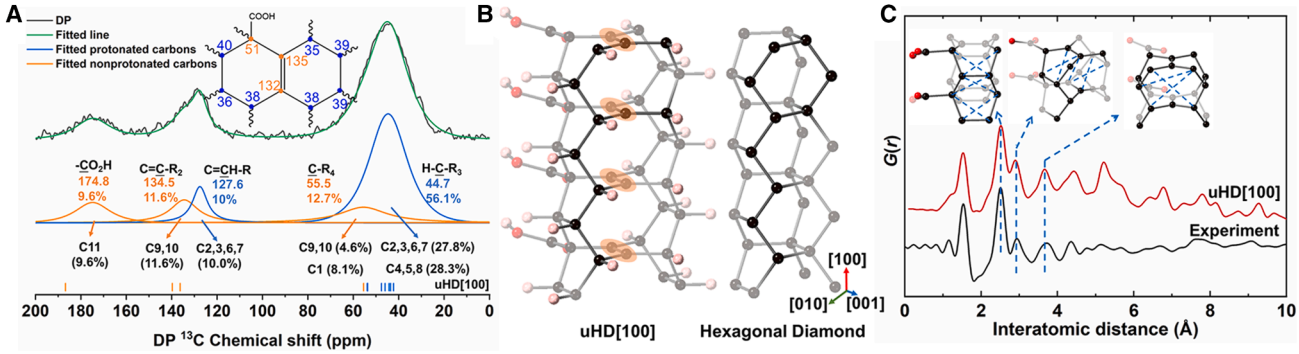

Figure 2. Local structure of the 1-NA CNTh and the polymerization process

(A) Quantitative ^{13}C ssNMR spectra of the 1-NA CNTh with fitted results. The blue and orange lines represent the fitted protonated and non-protonated carbons, respectively. The assignment of five peaks and the content are also presented. Vertical bars represent the calculated chemical shift of uHD[100].

(B) The structure of the uHD[100] (left) and HD fragment along [100] for comparison (right). The unsaturated atoms in uHD[100] are highlighted by the orange shadow.

(C) X-ray PDF pattern of PE20 and the simulated $G(r)$ of uHD[100] CNTh models.

PDF is also a powerful tool for determining the short-range structure. The X-ray total scattering data of PE20 and the simulated PDF pattern of uHD[100] are shown in Figure 2C. They show that uHD[100] reproduced the experimental data well. The peaks at 1.5, 2.4, 3.0, and 3.8 Å are perfectly recognizable as the distances between the carbon atom and its neighbor, the next neighbor, the third closest neighbor in the hexagonal ring, and the fourth neighbor in the octagonal ring, respectively, which again demonstrates the uHD[100] structure. Next, we constructed the crystal structure of 1-NA-CNTh on the basis of the intrathread structure of uHD[100] and the stacking of 1-NA and optimized it theoretically at 0 GPa and 0 K (see the methods for more details). It has lattice parameters of a = 7.23 Å, c = 29.97 Å, and β = 91.17°, in excellent agreement with the experimental data of a = 7.44 Å, c = 29.84 Å, and β = 92° (after thermal correction by 3.5%). Therefore, we confirmed that 1-NA CNThs are very orderly stacked and that uHD[100] represents the intrathread structure well.

Measurement of anisotropic compressibility and thermal conductivity

Because of the 1D characteristic of CNThs, we concentrated on the related anisotropic properties. Comparable to diamonds, CNThs are predicted to have an ultrahigh elastic modulus along the thread, so we measured the compressibility of the 1-NA CNTh single crystal by X-ray computed tomography under hydrostatic pressure. Figure 3A shows the projection of the 1-NA CNTh crystal on the *bc*-plane at 1.6 and 5.5 GPa. The length along the *b* axis (CNTh axis; Figure 3A) is nearly unchanged throughout the whole process, indicating high stiffness, whereas significant compression occurs along the *c* axis with a linear compressibility of 0.013 GPa^{-1}. Obviously, the sp^3 C–C bonds along the CNTh are highly resistant to compression, whereas van der Waals (vdW) interactions along the *c* axis are more compressible. A large elastic modulus along the direction of the CNTh can be expected. By contrast, carbon nanotubes are expected to have a high modulus of elasticity along the tube direction, whereas the radial cross-section of carbon nanotubes changes from circular to elliptical and then to a peanut shape, and it finally collapses under high pressure.[45–47]

The rigid sp^3 C–C bond network along the CNTh also suggests high thermal conductivity. We measured the anisotropic thermal conductivity of the 1-NA CNTh crystal by using time-domain thermoreflectance (TDTR), which is widely applied to extract thermal properties for diverse materials.[48–54] As shown in Figures 3B–3D, the thermal conductivities were $\Lambda_{a,CNTh}$ = 7.6 ± 1.5 W m^{-1} K^{-1}, $\Lambda_{b,CNTh}$ = 11.2 ± 0.9 W m^{-1} K^{-1} (along the thread), and $\Lambda_{c,CNTh}$ = 0.133 ± 0.008 W m^{-1} K^{-1} at room temperature. The thermal conductivity of the thread direction (*b* axis; Figure 3D) was very close to the theoretical calculation results of the tube (3,0) DNT-55 (length = ~24 nm; ~35.6 ± 4.7 W m^{-1} K^{-1}) and the tube (3,0) DNT forest (length = 18 nm).[55,56] For the thermal conductivity of the perpendicular direction (*c* axis; Figure 3B), $\Lambda_{c,CNTh}$ was in reasonable agreement with the calculated result of the DNT forest (0.22 W m^{-1} K^{-1}), which was restrained by vdW interactions.[56] The thermal conductivity along the thread was 84 times greater than the perpendicular direction ($\Lambda_{c,CNTh}$), which was highly anisotropic. This anisotropy, even if currently in an orderly stacked bulk crystal, is comparable to that of hexagonal boron nitride, which has a thermal conductivity anisotropy ratio of ρ = 87.5 at room temperature,[44] and exceeds the experimentally measured values of 1.2–13.5 for super-aligned carbon nanotube films.[57] This intrinsically large anisotropy is attributed to the distinct bonding type along these two heat flow directions. Mainly intermolecular vdW interactions occur along the *c* axis, whereas there is a C–C covalent bond along the thread, which facilitates the heat transfer and results in high thermal conductivity. If the interthread thermal conduction along the *c* axis is further disturbed with a suitable fabrication process, as in the study by Kim et al.,[58] it would be an even more promising material for devices requiring anisotropic thermal transport.

DISCUSSION

In conclusion, we synthesized a 100 μm single-crystal CNTh via topochemical polymerization of 1-NA under 20 GPa and 573 K.

Please cite this article in press as: Yang et al., Synthesis of single-crystalline carbon nanothreads from 1-naphthoic acid with high anisotropic thermal conductivity, Chem (2025), https://doi.org/10.1016/j.chempr.2025.102836

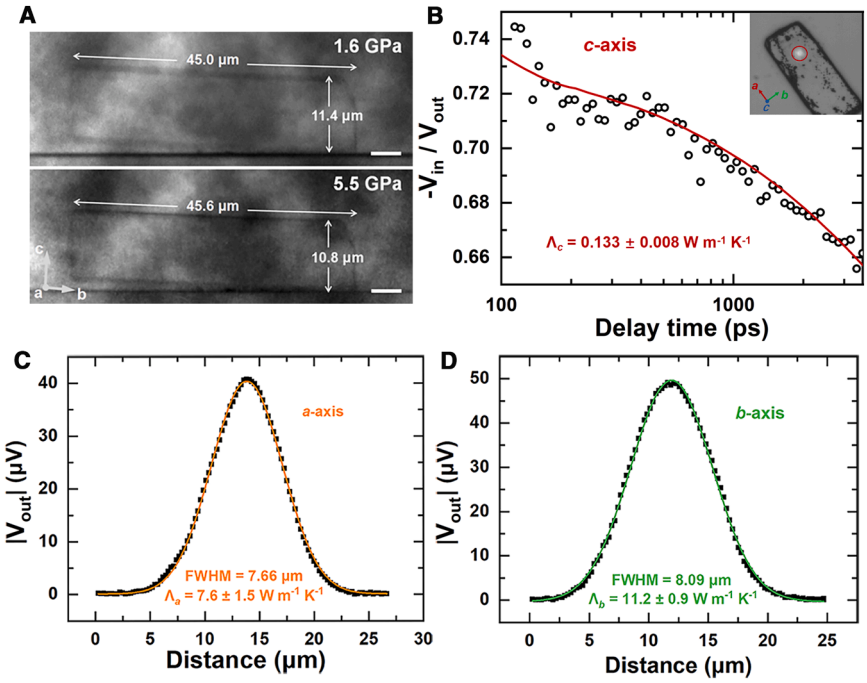

Figure 3. Compressibility and thermal conductivity of the 1-NA CNTh crystal

(A) *In situ* X-ray computed tomography images of the 1-NA CNTh crystal projected on the *b*-*c* plane at 1.6 GPa (crystal length along the *b* axis: 45.0 μm; along the *c* axis: 11.4 μm), 5.5 GPa (*b* axis: 45.6 μm; *c* axis: 10.8 μm). Scale bar: 5 μm.

(B) TDTR data of 1-NA CNTh along the *c* axis at room temperature. We fitted the experimental data (black circles) by using a diffusive multilayer thermal model to obtain the Λ_c (red solid line). The inset shows the single-crystal sample being measured.

(C and D) Beam-offset experimental data for 1-NA CNTh with the full width at half maximum (FWHM) determined from the fitted Gaussian function (curves). The offset direction is along the *a* axis (C) and *b* axis (D) of 1-NA CNTh.

It shows a periodic interthread arrangement with an unsaturated HD[100] intrathread structure. The suitable-slip π-π stacking and the distinct reaction activity of the carbon atoms (α- > β- > γ-) lead to an ordered intrathread structure, and the strong hydrogen bonds lock the CNTh in the crystalline lattice. These factors and the strategy of slow compression with annealing are the keys to this single-crystal-to-single-crystal transformation. The obtained 1-NA CNTh single crystal shows obvious anisotropic thermal conductivity and compressibility. Our work demonstrates that CNThs can be prepared as single crystals with good crystallinity, providing important insight for designing and synthesizing advanced diamond nanostructures under high pressure. The anisotropic properties evidenced by this experiment, especially the high anisotropic thermal conductivity, inspire a fresh perspective for exploring the properties and applications of CNThs for anisotropic thermal conductors.

METHODS

Synthesis of single- and poly-crystal 1-NA CNThs

1-NA (98%) was purchased from Macklin and purified by recrystallization in ethanol. The purity of 1-NA was examined via Rietveld refinement on the powder XRD collected on a Panalytical Empyrean diffractometer (Cu K_α radiation, λ = 1.5418 Å), and no impurities were detected. Single crystals of 1-NA were grown in an ethanol solution by slow volatilization. A 1-NA single crystal with neon pressure-transmitting medium was loaded into a symmetric DAC with a culet diameter of 400 μm. The DAC was compressed manually at 1 GPa/h to 20 GPa. It was then placed in an oven and kept at 573 K for 3 h of annealing. Then, it was gradually cooled to room temperature and decompressed to ambient pressure.

The sample PE20 was synthesized with a VX3 PE press, which was driven by an automatic hydraulic oil syringe pump. Double-toroidal sintered diamond anvils with a 4 mm dimple diameter were used for generating the pressure. Non-encapsulated T301 stainless steel gaskets were used, and the sample volume was 16.8 mm^3. The oil pressure was quickly increased to 100 bar (~1 GPa on the sample) to seal the sample and finally reached 1,600 bar, which was around 20 GPa according to the Edinburgh group calibration curve.[59] The rates during compression were as follows: 5 bar/min from 100 to 400 bar, 4 bar/min from 400 to 800 bar, 3 bar/min from 800 to 1,000 bar, 2 bar/min from 1,000 to 1,200 bar, 1 bar/min from 1,200 to 1,400 bar, and 0.5 bar/min from 1,400 to 1,600 bar. All samples were maintained at the target pressure for about 12 h and then decompressed to ambient pressure at the same rates as the compression process. The unreacted 1-NA in PE20 was dissolved and removed by ethanol.

Characterization of the 1-NA CNTh single crystal via XRD, TEM, and AFM

The lab single-crystal XRD experiments were performed on a Bruker D8 Venture with Mo K_α radiation (λ = 0.71073 Å), and the beam diameter was about 110 μm. APEX3 software was used for data collecting, spot finding, unit-cell determination, and indexing. High-resolution transmission electron microscopy (TEM) and SAED patterns were recorded on a JEM-2000 under a voltage of 200 kV. AFM experiments were performed on an Oxford Asylum Research Cypher ES AFM. The 1-NA CNTh single crystal was put on a mica surface. The images were collected under the atmosphere in tapping mode with a Multi75Al tip.

Characterization of product PE20 by XRD, X-ray PDF, and ssNMR

The powder XRD data of PE20 were collected on a Panalytical Empyrean diffractometer with monochromatized Cu K_α (λ = 1.5418 Å) radiation. Topas V6 software was used for performing the Rietveld refinements.[60]

Please cite this article in press as: Yang et al., Synthesis of single-crystalline carbon nanothreads from 1-naphthoic acid with high anisotropic thermal conductivity, Chem (2025), https://doi.org/10.1016/j.chempr.2025.102836

The synchrotron X-ray PDF experiment of PE20 was performed at the 11-ID-B beamline of the Advanced Photon Source at the Argonne National Laboratory. The powder sample (~10 mg) was loaded into a polyimide capillary. The incident X-ray beam was monochromatized to a wavelength of 0.2115 Å, and the instrument was calibrated by CeO_2. Dioptas software was used for reducing the collected 2D data and subtracting the background of an empty capillary.[61] The $G(r)$ data were reduced by PDF getX3 software, and the PDFgui software package was used for simulating the PDF data.[62]

The ^{13}C CP magic angle spinning (MAS) with total sideband suppression (TOSS) ssNMR experiments were recorded on a Bruker Avance III 400 MHz NMR spectrometer. The measurements were conducted with a Bruker 4.0 mm double resonance MAS NMR probe with 4 mm ZrO_2 rotors. The contact time (CT) and the MAS frequency were 800 μs and 8 kHz, respectively. The spectrum was acquired with a recycling delay of 1 s, averaging 6,144 scans. ^{13}C CPTOSS NQS spectrum was obtained through the addition of a dipolar dephasing delay of 60 μs to suppress the non-quaternary carbon peaks. The quantitative ^{13}C high-power proton decoupling spectrum was measured with a recycling delay of 120 s and averaged 723 scans. The ^{13}C chemical shifts were internally referenced to the methylene carbon of adamantane centered at 38.48 ppm. All the ssNMR spectra were analyzed by Topspin software and fitted with PeakFit software with the Gauss*Lorentz function.

^{1}H-^{13}C various CT CPMAS ssNMR experiments were performed with a Chemagnetics Infinity instrument. These employed a 4 μs 90° pulse on ^{1}H followed by spin locking ^{1}H and ^{13}C with a ramp in radio frequency (RF) amplitude on the ^{13}C channel for 4.5 ms. The recycling delay was 2 s. CT varied from 1 to 8 ms (ΔCT = 1 ms), and the number of acquisitions was 4,000 per CT value. The MAS was performed at 11.5 kHz. The curves were fitted with the following equation[63]:

$$I_t = I_0\left\{\exp\left(\frac{-t}{T_{1\rho}(\mathrm{H})}\right) - \exp\left(\frac{-t}{T_{\mathrm{CH}}}\right)\right\},$$

where t is the CT, $T_{1\rho}(H)$ is the time constant for the loss of spin-locked magnetization, T_{CH} is the time constant for polarization from ^{1}H to ^{13}C, I_t is the integrated intensity of the peak, and I_0 is the actual intensity of the peak.

In situ high-pressure IR, PL, UV-vis spectra, and XRD experiments

The *in situ* high-pressure IR, ultraviolet-visible (UV-vis), photoluminescence (PL), and powder XRD experiments were performed with a symmetric DAC with an anvil culet size of 400 μm in diameter. Type IIa diamond anvils were used in the IR, UV-vis, and PL experiments. The sample was loaded into holes with d = 180 μm drilled into the T-301 stainless steel gaskets, which were pre-indented to 30–40 μm thick. The pressure was determined via measurement of the ruby fluorescence according to the equation P (GPa) = 248.4[$(\lambda/\lambda_0)^{7.665} - 1$].[64]

The powder sample was loaded into the DAC for the *in situ* IR and *in situ* high-pressure synchrotron powder XRD experiments, and no pressure-transmitting medium was used in the measurements. For the *in situ* IR spectra of 1-NA single crystal, the single-crystal sample (~10 μm in thickness) was loaded in the DAC with neon as a pressure-transmitting medium. The Mid-IR experiment was performed in transmission mode at 600–4,000 cm^{-1} on a Bruker VERTEX 70v Fourier transform infrared (FTIR) spectrometer and a HYPERION 2000 microscope. A Globar was used as a conventional source. The resolution was 2 cm^{-1}, and the 20 × 20 μm^2 aperture for selecting the measured sample area. The spectra of an empty DAC at ambient pressure in the same aperture region were used as the background. For the *in situ* IR spectra of single-crystal 1-NA, the DAC was compressed manually to 20 GPa. It was then placed in an oven and kept at 573 K for annealing 3 h. After that, it was gradually cooled to room temperature for measurement of the IR spectra.

The UV-vis absorption spectra, PL, and optical images of the single-crystal sample were collected in a home-designed spectroscopy system in a micro-region (Gora-UVN-FL, built by Ideaoptics, Shanghai, China). Silicone oil was used as the pressure-transmitting medium for the UV-vis and PL measurements. The *in situ* UV-vis absorption spectra were collected with a xenon light source between 200 and 1,700 nm. The UV-vis spectra of the silicone oil area at each pressure point were used as the background. The PL spectra were measured with a 360 nm laser.

The *in situ* high-pressure synchrotron powder XRD experiments were performed at the 4W2 beamline of the Beijing Synchrotron Radiation Facility with a 20 × 30 μm^2 beam size. The incident X-ray beam was monochromatized to a wavelength of 0.6199 Å, and the instrument was calibrated by CeO_2. The diffraction patterns were collected with a Pilatus 2M detector. Dioptas software[61] was used for reducing the collected data, and Jana 2006 software[65] was used for Le Bail fitting and Rietveld refinements.

TDTR and high-pressure *in situ* X-ray computed tomography

TDTR was performed according to the detailed information provided by Cahill[48] and Sun and Koh.[49] Before the experiment, its volumetric heat capacity was determined to be $C_{V,CNTh}$ = 1.87 J cm^{-3} K^{-1} at 300 K. An aluminum layer of 90 nm thickness was deposited on the sample as a transducer by magnetron sputtering. During the experiment, we split the pulsed femtosecond laser (785 nm, 80 MHz repetition rate) into the pump and probe beams by using a polarizing beam splitter. To measure thermal conductivity perpendicular to the basal plane Λ_c, we used a $1/e^2$ beam radius of 12 μm. The pump beam was modulated at 10.1 MHz so that the temperature gradient was mainly 1D along the c axis.

To measure the in-plane thermal conductivities, we used a laser with a smaller radius of 3 μm and a lower modulating frequency of 0.21 MHz to heat the sample and generate periodic temperature oscillations on the sample surface. We measured the thermal conductivity along the a axis ($\Lambda_{a,CNTh}$) and b axis ($\Lambda_{b,CNTh}$) with offsetting pump and probe laser spots along the corresponding directions.[50] To reduce the experimental uncertainty of our TDTR measurements along the a and b axes, we deposited an 80-nm-thick bismuth layer instead of an Al layer on the sample by vacuum evaporation. We modulated the probe beam at 200 Hz to improve

the signal-to-noise ratio and monitored the temperature-dependent reflectance change from the surface.

High-pressure *in situ* X-ray computed tomography was performed on an Xradia 800Ultra X-ray Microscope. Before the experiment, a 1-NA CNTh crystal with a size of $24 \times 45 \times 11\ \mu m^3$ was coated with a layer of gold. We used silicone oil as a pressure medium, beryllium as a gasket to allow X-rays to penetrate, and a custom DAC with a culet diameter of 300 μm for compression. The computed tomography images of the 1-NA CNTh crystal at 1.6 GPa (the pixel size is $63.33 \times 63.33\ nm^2$) and 5.5 GPa (the pixel size is $126.66 \times 126.66\ nm^2$) were collected. The sample was rotated in the instrument, and one image was collected for every 0.2° of rotation. We selected the clearest image of the sample edge to measure the changes in the length, width, and height of the sample under high pressure and calculated the anisotropic compression of the sample. The compressibility per unit pressure (C) was calculated by the following formula:

$$C = \frac{l_0 - l_P}{l_0} \Big/ \Delta P,$$

where l_0 and l_P are the initial and compressed sizes of the sample, respectively, and ΔP is the applied pressure.

DFT calculations

We performed density functional theory (DFT) calculations to investigate the polymerization of 1-NA in the Cambridge Sequential Total Energy Package (CASTEP) code.[66] The critical structure of 1-NA at 14.7 GPa was optimized with a space group $P2_1/c$ lattice (a = 6.37 Å, b = 3.14 Å, c = 28.84 Å, β = 92.88°) on the basis of the *in situ* XRD experiment. The local density approximation (LDA) with the Ceperley-Alder-Perdew-Zunger (CA-PZ) exchange-correlation functional was used,[67] as well as the ultrasoft pseudopotentials. The cutoff energy was set as 630 eV, and the k-point solution was better than $0.05 \times 2\pi\ A^{-1}$.

The crystal structure of uHD[100] CNTh was built with a unit cell containing four CNThs. Then, it was optimized with variable lattice parameters in Material Studio software with the geometry optimization of the focite module and CASTEP module on the basis of the crystal structure of 1-NA at 14.7 GPa.

The simulated chemical shielding constants of the uHD[100] CNTh model were also calculated by CASTEP.[68] Local density approximation with Ceperley-Alder correlation parameterized by Perdew and Zunger (LDA-CA-PZ) with on-the-fly generation (OTFG) norm-conserving pseudopotentials was implemented with a 990 eV energy cutoff. The chemical shifts were calculated as

$$\delta^{calc}_{CNTh} = \sigma^{calc}_{ref} + \delta^{exp}_{ref} - \sigma^{calc}_{CNTh},$$

where σ^{calc}_{CNTh} and σ^{calc}_{ref} are the simulated chemical shielding of the CNTh model and the reference compound (adamantane), respectively. The δ^{exp}_{ref} is the experimental chemical shift of reference (methylene carbon of adamantane at 38.48 ppm).

RESOURCE AVAILABILITY

Lead contact

Requests for further information and resources should be directed to and will be fulfilled by the lead contact, Kuo Li (likuo@hpstar.ac.cn).

Materials availability

The compounds generated in this study are available from the lead contact upon reasonable request.

Data and code availability

All data needed to support the conclusions of this manuscript are included in the main text or the supplemental information.

ACKNOWLEDGMENTS

The authors acknowledge the support of the National Key Research and Development Program of China (2023YFA1406200) and the National Natural Science Foundation of China (22022101). This study was also partially supported by the Synergetic Extreme Condition User Facility (SECUF). The *in situ* XRD measurements were carried out with the support of the 4W2 beamline at the Beijing Synchrotron Radiation Facility and the 15U and BL17UM beamlines at the Shanghai Synchrotron Radiation Facility. The PDF data were collected at the 11-ID-B beamline of the Advanced Photon Source at the Argonne National Laboratory and the 13HB beamline of the Shanghai Synchrotron Radiation Facility. The authors thank Dr. Yanpeng Qi for his helpful discussions of thermal conductivity measurement; Dr. Dongliang Yang and Dr. Chengwen Mao for their assistance with *in situ* XRD measurements under high pressure; Dr. Xujie Lü for supporting the *in situ* UV-vis, PL, and imaging measurements; Dr. Hongliang Dong for supporting the PDF experiments; Baihua Chen for assisting with the powder XRD experiments; Dr. Xiaoge Wang and Dr. Jing Ju for supporting the TEM experiments; Dr. Zhisheng Zhao for his helpful discussions; Dr. Yali Qiao, Yongrui Yang, and Lutong Guo for helping with depositing the bismuth layer; Dr. Hong Xiao, Qi Feng, and Meilun Li for supporting the volumetric heat capacity experiments; Dr. Fuyang Liu for assisting with the SCXRD experiments; and Dr. Jiangjun Li for supporting the AFM experiments.

AUTHOR CONTRIBUTIONS

X.Y. and Q.Z. performed the synthesis and structural characterization research; Q.Z. synthesized the single-crystal products for the TDTR experiments and performed the computed tomography experiments; Y.L. and B.S. conducted the TDTR experiments; R.S. helped to perform the *in situ* single-crystal experiment and synthesize the single-crystal products; X.Y., X.T., and X.D. performed the theoretical calculations; X.Y., G.C., P.Z., and Y.C. performed the TEM experiments; A.G., J.X., and G.D.C. performed the ssNMR experiments; H.Z. helped to analyze the ssNMR data; Yida Wang and X.W. helped to collect the *in situ* XRD data; D.G. and Yajie Wang helped to analyze the *in situ* XRD data; H.-k.M. provided partial funding support; K.L. proposed and supervised the whole project and helped to analyze the XRD and TEM data; and X.Y., Q.Z., and K.L. wrote the manuscript with contributions from all authors.

DECLARATION OF INTERESTS

The authors declare no competing interests.

SUPPLEMENTAL INFORMATION

Supplemental information can be found online at https://doi.org/10.1016/j.chempr.2025.102836.

Received: May 4, 2025
Revised: August 23, 2025
Accepted: November 3, 2025

REFERENCES

1. Chaudhri, M.M. (2020). Indentation hardness of diamond single crystals, nanopolycrystal, and nanotwinned diamonds: A critical review.

Diam. Relat. Mater. *109*, 108076. https://doi.org/10.1016/j.diamond.2020.108076.

2. Olson, J.R., Pohl, R.O., Vandersande, J.W., Zoltan, A., Anthony, T.R., and Banholzer, W.F. (1993). Thermal conductivity of diamond between 170 and 1200 K and the isotope effect. Phys. Rev. B Condens. Matter *47*, 14850–14856. https://doi.org/10.1103/PhysRevB.47.14850.
3. Isberg, J., Hammersberg, J., Johansson, E., Wikström, T., Twitchen, D.J., Whitehead, A.J., Coe, S.E., and Scarsbrook, G.A. (2002). High carrier mobility in single-crystal plasma-deposited diamond. Science *297*, 1670–1672. https://doi.org/10.1126/science.1074374.
4. Wort, C.J.H., and Balmer, R.S. (2008). Diamond as an electronic material. Mater. Today *11*, 22–28. https://doi.org/10.1016/S1369-7021(07)70349-8.
5. Yang, W., Auciello, O., Butler, J.E., Cai, W., Carlisle, J.A., Gerbi, J.E., Gruen, D.M., Knickerbocker, T., Lasseter, T.L., Russell, J.N., Jr., et al. (2002). DNA-modified nanocrystalline diamond thin-films as stable, biologically active substrates. Nat. Mater. *1*, 253–257. https://doi.org/10.1038/nmat779.
6. Sorokin, P.B., and Yakobson, B.I. (2021). Two-dimensional diamond-diamane: Current state and further prospects. Nano Lett. *21*, 5475–5484. https://doi.org/10.1021/acs.nanolett.1c01557.
7. Roman, R.E., Kwan, K., and Cranford, S.W. (2015). Mechanical properties and defect sensitivity of diamond nanothreads. Nano Lett. *15*, 1585–1590. https://doi.org/10.1021/nl5041012.
8. Stojkovic, D., Zhang, P., and Crespi, V.H. (2001). Smallest nanotube: Breaking the symmetry of sp^3 bonds in tubular geometries. Phys. Rev. Lett. *87*, 125502. https://doi.org/10.1103/PhysRevLett.87.125502.
9. Fitzgibbons, T.C., Guthrie, M., Xu, E.S., Crespi, V.H., Davidowski, S.K., Cody, G.D., Alem, N., and Badding, J.V. (2015). Benzene-derived carbon nanothreads. Nat. Mater. *14*, 43–47. https://doi.org/10.1038/nmat4088.
10. Xu, E.S., Lammert, P.E., and Crespi, V.H. (2015). Systematic enumeration of sp^3 nanothreads. Nano Lett. *15*, 5124–5130. https://doi.org/10.1021/acs.nanolett.5b01343.
11. Zhu, T., and Ertekin, E. (2016). Phonons, localization, and thermal conductivity of diamond nanothreads and amorphous graphene. Nano Lett. *16*, 4763–4772. https://doi.org/10.1021/acs.nanolett.6b00557.
12. Zhan, H., Zhang, G., Bell, J.M., and Gu, Y. (2016). The morphology and temperature dependent tensile properties of diamond nanothreads. Carbon *107*, 304–309. https://doi.org/10.1016/j.carbon.2016.06.006.
13. Duan, K., Li, Y., Li, L., Hu, Y., and Wang, X. (2018). Diamond nanothread based resonators: ultrahigh sensitivity and low dissipation. Nanoscale *10*, 8058–8065. https://doi.org/10.1039/c8nr00502h.
14. Zhan, H., Zhang, G., Tan, V.B.C., Cheng, Y., Bell, J.M., Zhang, Y.W., and Gu, Y. (2016). Diamond nanothread as a new reinforcement for nanocomposites. Adv. Funct. Mater. *26*, 5279–5283. https://doi.org/10.1002/adfm.201600119.
15. Zhan, H., Zhang, G., Bell, J.M., Tan, V.B.C., and Gu, Y. (2020). High density mechanical energy storage with carbon nanothread bundle. Nat. Commun. *11*, 1905. https://doi.org/10.1038/s41467-020-15807-7.
16. Zhan, H., Zhang, G., Tan, V.B.C., and Gu, Y. (2017). The best features of diamond nanothread for nanofibre applications. Nat. Commun. *8*, 14863. https://doi.org/10.1038/ncomms14863.
17. Li, X., Baldini, M., Wang, T., Chen, B., Xu, E.-S., Vermilyea, B., Crespi, V.H., Hoffmann, R., Molaison, J.J., Tulk, C.A., et al. (2017). Mechanochemical synthesis of carbon nanothread single crystals. J. Am. Chem. Soc. *139*, 16343–16349. https://doi.org/10.1021/jacs.7b09311.
18. Duan, P., Li, X., Wang, T., Chen, B., Juhl, S.J., Koeplinger, D., Crespi, V.H., Badding, J.V., and Schmidt-Rohr, K. (2018). The chemical structure of carbon nanothreads analyzed by advanced solid-state NMR. J. Am. Chem. Soc. *140*, 7658–7666. https://doi.org/10.1021/jacs.8b03733.
19. Juhl, S.J., Wang, T., Vermilyea, B., Li, X., Crespi, V.H., Badding, J.V., and Alem, N. (2019). Local structure and bonding of carbon nanothreads probed by high-resolution transmission electron microscopy. J. Am. Chem. Soc. *141*, 6937–6945. https://doi.org/10.1021/jacs.8b13405.
20. Chen, B., Hoffmann, R., Ashcroft, N.W., Badding, J., Xu, E.-S., and Crespi, V. (2015). Linearly polymerized benzene arrays as intermediates, tracing pathways to carbon nanothreads. J. Am. Chem. Soc. *137*, 14373–14386. https://doi.org/10.1021/jacs.5b09053.
21. Huss, S., Wu, S., Chen, B., Wang, T., Gerthoffer, M.C., Ryan, D.J., Smith, S.E., Crespi, V.H., Badding, J.V., and Elacqua, E. (2021). Scalable synthesis of crystalline one-dimensional carbon nanothreads through modest-pressure polymerization of furan. ACS Nano *15*, 4134–4143. https://doi.org/10.1021/acsnano.0c10400.
22. Biswas, A., Ward, M.D., Wang, T., Zhu, L., Huang, H.-T., Badding, J.V., Crespi, V.H., and Strobel, T.A. (2019). Evidence for orientational order in nanothreads derived from thiophene. J. Phys. Chem. Lett. *10*, 7164–7171. https://doi.org/10.1021/acs.jpclett.9b02546.
23. Gao, D., Tang, X., Xu, J., Yang, X., Zhang, P., Che, G., Wang, Y., Chen, Y., Gao, X., Dong, X., et al. (2022). Crystalline $C_3N_3H_3$ tube (3,0) nanothreads. Proc. Natl. Acad. Sci. USA *119*, e2201165119. https://doi.org/10.1073/pnas.2201165119.
24. Li, X., Wang, T., Duan, P., Baldini, M., Huang, H.-T., Chen, B., Juhl, S.J., Koeplinger, D., Crespi, V.H., Schmidt-Rohr, K., et al. (2018). Carbon nitride nanothread crystals derived from pyridine. J. Am. Chem. Soc. *140*, 4969–4972. https://doi.org/10.1021/jacs.7b13247.
25. Dunning, S.G., Zhu, L., Chen, B., Chariton, S., Prakapenka, V.B., Somayazulu, M., and Strobel, T.A. (2022). Solid-state pathway control via reaction-directing heteroatoms: ordered pyridazine nanothreads through selective cycloaddition. J. Am. Chem. Soc. *144*, 2073–2078. https://doi.org/10.1021/jacs.1c12143.
26. Ward, M.D., Tang, W.S., Zhu, L., Popov, D., Cody, G.D., and Strobel, T.A. (2019). Controlled single-crystalline polymerization of $C_{10}H_8{\cdot}C_{10}F_8$ under pressure. Macromolecules *52*, 7557–7563. https://doi.org/10.1021/acs.macromol.9b01416.
27. Friedrich, A., Collings, I.E., Dziubek, K.F., Fanetti, S., Radacki, K., Ruiz-Fuertes, J., Pellicer-Porres, J., Hanfland, M., Sieh, D., Bini, R., et al. (2020). Pressure-induced polymerization of polycyclic arene-perfluoroarene cocrystals: Single crystal X-ray diffraction studies, reaction kinetics, and design of columnar hydrofluorocarbons. J. Am. Chem. Soc. *142*, 18907–18923. https://doi.org/10.1021/jacs.0c09021.
28. Gerthoffer, M.C., Wu, S., Chen, B., Wang, T., Huss, S., Oburn, S.M., Crespi, V.H., Badding, J.V., and Elacqua, E. (2020). 'Sacrificial' supramolecular assembly and pressureinduced polymerization: Toward sequence-defined functionalized nanothreads. Chem. Sci. *11*, 11419–11424. https://doi.org/10.1039/d0sc03904g.
29. Yang, X., Che, G., Wang, Y., Zhang, P., Tang, X., Lang, P., Gao, D., Wang, X., Wang, Y., Hattori, T., et al. (2025). High-pressure polymerization of phenol toward degree-4 carbon nanothread. Nano Lett. *25*, 1028–1035. https://doi.org/10.1021/acs.nanolett.4c04895.
30. Nobrega, M.M., Teixeira-Neto, E., Cairns, A.B., Temperini, M.L.A., and Bini, R. (2018). One-dimensional diamondoid polyaniline-like nanothreads from compressed crystal aniline. Chem. Sci. *9*, 254–260. https://doi.org/10.1039/c7sc03445h.
31. Wang, X., Yang, X., Wang, Y., Tang, X., Zheng, H., Zhang, P., Gao, D., Che, G., Wang, Z., Guan, A., et al. (2022). From biomass to functional crystalline diamond nanothread: Pressure-induced polymerization of 2,5-furandicarboxylic acid. J. Am. Chem. Soc. *144*, 21837–21842. https://doi.org/10.1021/jacs.2c08914.
32. Dunning, S.G., Chen, B., Zhu, L., Cody, G.D., Chariton, S., Prakapenka, V.B., Zhang, D., and Strobel, T.A. (2023). Synthesis and post-processing of chemically homogeneous nanothreads from 2,5-furandicarboxylic acid. Angew. Chem. Int. Ed. *62*, e202217023. https://doi.org/10.1002/anie.202217023.
33. Murphy, M., Mohamed, A., Badding, J.V., and Elacqua, E. (2025). Rational approaches toward the design and synthesis of carbon nanothreads. Acc. Chem. Res. *58*, 2191–2202. https://doi.org/10.1021/acs.accounts.5c00172.

34. Demingos, P.G., and Muniz, A.R. (2018). Carbon nanothreads from polycyclic aromatic hydrocarbon molecules. Carbon *140*, 644–652. https://doi.org/10.1016/j.carbon.2018.09.022.

35. Silveira, J.F.R.V., and Muniz, A.R. (2018). Diamond nanothread-based 2D and 3D materials: Diamond nanomeshes and nanofoams. Carbon *139*, 789–800. https://doi.org/10.1016/j.carbon.2018.07.021.

36. Tang, W.S., and Strobel, T.A. (2020). Evidence for functionalized carbon nanothreads from π-stacked, para-disubstituted benzenes. J. Phys. Chem. C *124*, 25062–25070. https://doi.org/10.1021/acs.jpcc.0c06715.

37. Funnell, N.P., Dawson, A., Marshall, W.G., and Parsons, S. (2013). Destabilisation of hydrogen bonding and the phase stability of aniline at high pressure. CrystEngComm *15*, 1047–1060. https://doi.org/10.1039/C2CE26403J.

38. Guo, Q.-H., Jia, M., Liu, Z., Qiu, Y., Chen, H., Shen, D., Zhang, X., Tu, Q., Ryder, M.R., Chen, H., et al. (2020). Single-crystal polycationic polymers obtained by single-crystal-to-single-crystal photopolymerization. J. Am. Chem. Soc. *142*, 6180–6187. https://doi.org/10.1021/jacs.9b13790.

39. Wang, M., Jin, Y., Zhang, W., and Zhao, Y. (2023). Single-crystal polymers (SCPs): From 1D to 3D architectures. Chem. Soc. Rev. *52*, 8165–8193. https://doi.org/10.1039/d3cs00553d.

40. Lauher, J.W., Fowler, F.W., and Goroff, N.S. (2008). Single-crystal-to-single-crystal topochemical polymerizations by design. Acc. Chem. Res. *41*, 1215–1229. https://doi.org/10.1021/ar8001427.

41. Zhao, W., Zhang, J., Sun, Z., Xiao, G., Zheng, H., Li, K., Li, M.-R., and Zou, B. (2025). Chemical synthesis driven by high pressure. CCS Chem. *7*, 1250–1271. https://doi.org/10.31635/ccschem.024.202405293.

42. Mao, H.-K., Chen, B., Gou, H., Li, K., Liu, J., Xiao, H., and Yang, W. (2024). 2023 HP special volume: Synergistic progress of high-pressure physics and chemistry. Matter Radiat. Extremes *9*, 063001. https://doi.org/10.1063/5.0244367.

43. Tang, X., Dong, X., Zhang, C., Li, K., Zheng, H., and Mao, H.-K. (2023). Triggering dynamics of acetylene topochemical polymerization. Matter Radiat. Extremes *8*, 058402. https://doi.org/10.1063/5.0151609.

44. Jiang, P., Qian, X., Yang, R., and Lindsay, L. (2018). Anisotropic thermal transport in bulk hexagonal boron nitride. Phys. Rev. Mater. *2*, 064005. https://doi.org/10.1103/PhysRevMaterials.2.064005.

45. Liew, K.M., and Sun, Y. (2008). Elastic properties and pressure-induced structural transitions of single-walled carbon nanotubes. Phys. Rev., B *77*, 205437. https://doi.org/10.1103/PhysRevB.77.205437.

46. Chen, C., Lin, Y., Zhou, W., Gong, M., He, Z., Shi, F., Li, X., Wu, J.Z., Lam, K.T., Wang, J.N., et al. (2021). Sub-10-nm graphene nanoribbons with atomically smooth edges from squashed carbon nanotubes. Nat. Electron. *4*, 653–663. https://doi.org/10.1038/s41928-021-00633-6.

47. Balima, F., Le Floch, S.L., Adessi, C., Cerqueira, T.F.T., Blanchard, N., Arenal, R., Brûlet, A., Marques, M.A.L., Botti, S., and San-Miguel, A. (2016). Radial collapse of carbon nanotubes for conductivity optimized polymer composites. Carbon *106*, 64–73. https://doi.org/10.1016/j.carbon.2016.05.004.

48. Cahill, D.G. (2004). Analysis of heat flow in layered structures for time-domain thermoreflectance. Rev. Sci. Instrum. *75*, 5119–5122. https://doi.org/10.1063/1.1819431.

49. Sun, B., and Koh, Y.K. (2016). Understanding and eliminating artifact signals from diffusely scattered pump beam in measurements of rough samples by time-domain thermoreflectance (TDTR). Rev. Sci. Instrum. *87*, 064901. https://doi.org/10.1063/1.4952579.

50. Feser, J.P., and Cahill, D.G. (2012). Probing anisotropic heat transport using time-domain thermoreflectance with offset laser spots. Rev. Sci. Instrum. *83*, 104901. https://doi.org/10.1063/1.4757863.

51. Liu, Y., Li, Q., Qian, Y., Yang, Y., Wang, S., Li, W., and Sun, B. (2023). Thermal conductivity of high-temperature high-pressure synthesized θ-TaN. Appl. Phys. Lett. *122*, 222201. https://doi.org/10.1063/5.0146492.

52. Liu, Y., Li, Q., Liu, F., Wang, X., and Sun, B. (2025). Boundary conditions dictate frequency dependence of thermal conductivity in silicon. Appl. Phys. Rev. *12*, 031421. https://doi.org/10.1063/5.0254248.

53. Liu, Y., and Sun, B. (2025). Electron tunneling enhances thermal conductance through metal-insulator-semiconductor junctions. Phys. Rev. Lett. *135*, 206304. https://doi.org/10.1103/1s3l-kv58.

54. Liu, Y., Zhou, X., Wang, S., and Sun, B. (2025). Thermal conductivity of polar nitride perovskite LaWN3. Modern Phys. Lett. B *39*, 2550052. https://doi.org/10.1142/S0217984925500526.

55. Zhan, H., Zhang, G., Zhang, Y., Tan, V.B.C., Bell, J.M., and Gu, Y. (2016). Thermal conductivity of a new carbon nanotube analog: The diamond nanothread. Carbon *98*, 232–237. https://doi.org/10.1016/j.carbon.2015.11.012.

56. Xue, Y., Chen, Y., Li, Z., Jiang, J.-W., Zhang, Y., and Wei, N. (2019). Strain engineering for thermal conductivity of diamond nanothread forests. J. Phys., D *52*, 085301. https://doi.org/10.1088/1361-6463/aaf559.

57. Yu, W., Zhao, X., Jiang, P., Liu, C., and Yang, R. (2021). Tunable anisotropic thermal transport in super-aligned carbon nanotube films. Mater. Today Phys. *20*, 100447. https://doi.org/10.1016/j.mtphys.2021.100447.

58. Kim, S.E., Mujid, F., Rai, A., Eriksson, F., Suh, J., Poddar, P., Ray, A., Park, C., Fransson, E., Zhong, Y., et al. (2021). Extremely anisotropic van der Waals thermal conductors. Nature *597*, 660–665. https://doi.org/10.1038/s41586-021-03867-8.

59. Hattori, T., Sano-Furukawa, A., Machida, S., Abe, J., Funakoshi, K., Arima, H., and Okazaki, N. (2019). Development of a technique for high pressure neutron diffraction at 40 GPa with a Paris-Edinburgh press. High Press. Res. *39*, 417–425. https://doi.org/10.1080/08957959.2019.1624745.

60. Coelho, A.A. (2018). TOPAS and TOPAS-academic: An optimization program integrating computer algebra and crystallographic objects written in C++. J. Appl. Crystallogr. *51*, 210–218. https://doi.org/10.1107/S1600576718000183.

61. Prescher, C., and Prakapenka, V.B. (2015). DIOPTAS: A program for reduction of two-dimensional X-ray diffraction data and data exploration. High Press. Res. *35*, 223–230. https://doi.org/10.1080/08957959.2015.1059835.

62. Farrow, C.L., Juhas, P., Liu, J.W., Bryndin, D., Božin, E.S., Bloch, J., Proffen, T., and Billinge, S.J.L. (2007). PDFfit2 and PDFgui: Computer programs for studying nanostructure in crystals. J. Phys. Condens. Matter *19*, 335219. https://doi.org/10.1088/0953-8984/19/33/335219.

63. Burgess, S.K., Leisen, J.E., Kraftschik, B.E., Mubarak, C.R., Kriegel, R.M., and Koros, W.J. (2014). Chain mobility, thermal, and mechanical properties of poly(ethylene furanoate) compared to poly(ethylene terephthalate). Macromolecules *47*, 1383–1391. https://doi.org/10.1021/ma5000199.

64. Mao, H.K., Xu, J., and Bell, P.M. (1986). Calibration of the ruby pressure Gauge to 800 kbar under quasi-hydrostatic conditions. J. Geophys. Res. *91*, 4673–4676. https://doi.org/10.1029/JB091iB05p04673.

65. Petříček, V., Dušek, M., and Palatinus, L. (2014). Crystallographic computing system JANA2006: General features. Z. Kristallogr. Cryst. Mater *229*, 345–352. https://doi.org/10.1515/zkri-2014-1737.

66. Clark, S.J., Segall, M.D., Pickard, C.J., Hasnip, P.J., Probert, M.I.J., Refson, K., and Payne, M.C. (2005). First principles methods using CASTEP. Z. Kristallogr. Cryst. Mater. *220*, 567–570. https://doi.org/10.1524/zkri.220.5.567.65075.

67. Perdew, J.P., and Zunger, A. (1981). Self-interaction correction to density-functional approximations for many-electron systems. Phys. Rev., B *23*, 5048–5079. https://doi.org/10.1103/PhysRevB.23.5048.

68. Bonhomme, C., Gervais, C., Babonneau, F., Coelho, C., Pourpoint, F., Azaïs, T., Ashbrook, S.E., Griffin, J.M., Yates, J.R., Mauri, F., et al. (2012). First-principles calculation of NMR parameters using the Gauge including projector augmented wave method: A chemist's point of view. Chem. Rev. *112*, 5733–5779. https://doi.org/10.1021/cr300108a.